WALL SHEAR STRESS GRADIENT ANALYSIS WITHIN AN IDEALIZED STENOSIS USING NON-NEWTONIAN FLOW

Clemens M. Schirmer, M.D.

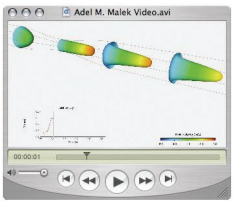
Cerebrovascular and
Endovascular Division,
Department of Neurosurgery,
Tufts–New England Medical Center and
Tufts University School of Medicine,
Boston, Massachusetts

Adel M. Malek, M.D., Ph.D.

Cerebrovascular and
Endovascular Division,
Department of Neurosurgery,
Tufts–New England Medical Center and
Tufts University School of Medicine,
Boston, Massachusetts

Reprint requests:
Adel M. Malek, M.D., Ph.D.,
Cerebrovascular and
Endovascular Division,
Department of Neurosurgery,
Tufts–New England Medical Center,
750 Washington Street, Box 178, Proger 7,
Boston, MA 02111.
Email: amalek@tufts-nemc.org

Received, September 8, 2006.
Accepted, January 8, 2007.



ONLINE DIGITAL VIDEO

OBJECTIVE: The endothelium is functionally regulated by the magnitude and spatiotemporal gradients of wall shear stress (WSS). Although flow separation and reversal occur beyond high-grade stenoses, little is known of the WSS pattern within clinically relevant mild to moderate stenoses.

METHODS: An axisymmetric geometry with 25, 50, and 75% stenosis criteria (quantified in accordance with the North American Symptomatic Carotid Endarterectomy Trial) was used to generate a high-resolution, hybrid, tetrahedral-hexahedral computational mesh with boundary-layer enrichment to improve near-wall shear stress gradient (WSSG) computation. Time-dependent computational fluid dynamic analysis was performed using a non-Newtonian Carreau-Yasuda model of blood to yield the shear-dependent viscosity.

RESULTS: Transition to secondary flow patterns was demonstrated in stenoses of 25, 50, and 75%. A focal region with near-wall flow reversal and retrograde WSS was identified within the stenosis itself and was found to migrate cyclically during the cardiac pulse. A zone of zero WSS and divergent WSSG that shifts in toward the throat with increasing stenotic severity was identified. Focal zones of high WSSG with converging and/or diverging direction were uncovered within the stenosis itself, as were expected changes in the distal poststenotic region. These zones of divergent WSSG shift over a substantial length of the stenosis during the course of the cardiac cycle.

CONCLUSION: Luminal WSS demonstrates dynamic direction reversal and high spatial gradients within the distal stenosis throat of even clinically moderate lesions. These findings shed light on the complex vessel wall hemodynamics within clinical stenoses and reveal a mechanical microenvironment that is conducive to perpetual endothelial functional dysregulation and stenosis progression.

KEY WORDS: Atherosclerosis, Endothelium, Fluid dynamics, Stenosis

Neurosurgery 61:853–864, 2007 DOI: 10.1227/01.NEU.0000280054.23770.3E www.neurosurgery-online.com

Wall shear stress (WSS) is known to regulate endothelial cell (EC) function and phenotype and may play a role in the progression of atherosclerosis (24, 27, 33). The exact temporal and spatial patterns of WSS remain poorly defined with regard to atherosclerotic lesions and stenotic sites because of the computational complexity involved in WSS determination (32, 44, 47). Although it is well known that secondary flow phenomena occur in critical stenosis with consequent flow reversal, there have been few studies of WSS in and around sites of mild- and moderate-grade stenoses (22). This is of increasing interest because ECs have been shown to be functionally regulated not only by overall WSS magnitude but also by WSS gradients (WSSGs) in time and space (4, 20). Physiological WSS (> 15 dyn/cm^2) leads to EC actin stress-fiber induction, cell change from polygonal to fusiform shape, and cell reorientation in the direction of flow (34). Physiological WSS induces a quiescent state by decreasing EC apoptosis and mitosis (17), downregulating EC expression of growth factors and monocyte adhesion molecules, and upregulating vasodilators such as nitric oxide synthase, antioxidant enzymes, and tissue plasminogen activator (33). In contrast, low WSS (< 4 dyn/cm^2) is associated with the opposite response and a phenotypically aggressive profile that possibly contributes to atherosclerosis progression (13, 43). WSS has also been implicated in mediating the intimal hyperplasia that occurs in coronary arteries after stenting, in which restenosis was identified in areas of low WSS, whereas regions exposed to physiological and elevated WSS were spared (3, 43). ECs have also been

shown to be sensitive not only to WSS magnitude but also to its spatial gradient with activation of transcription factors nuclear factor-κB, Egr-1, c-Jun, and c-Fos (37); increased mitosis; and increased permeability (39). Temporal gradients and time-varying WSS, even in the absence of a spatial WSSG, also have a significant effect on EC function when compared with steady WSS (14, 35).

Previous biomechanical studies have focused on defining the pattern of blood flow within a stenotic vessel; however, most studies have lacked the resolution to adequately estimate the shear forces on the endothelium (7, 9, 28, 30). We sought to characterize the shear forces in both space and time within a smooth, idealized axisymmetric geometry using computational fluid dynamics (CFD) modeling with a high-resolution computational mesh and a realistic non-Newtonian Carreau-Yasuda formulation of blood viscosity. This approach has enabled us to evaluate the fluid dynamics within the region of the stenosis by providing a high-resolution representation of the stenosis itself. This contrasts with previous approaches, which have focused on poststenotic regions. Most of these studies assumed a nonrealistic, sudden-expansion model of stenosis, which prevented detailed analysis of the hemodynamic environment within the stenosis itself and focused primarily on the poststenotic region. The present approach enables the computation of wall shear forces and their spatiotemporal characteristics within the throat of the stenosis and the poststenotic region, and thus allows for the parametric evaluation of increasing degrees of stenosis and flow velocities.

We demonstrate the presence of a region within the stenosis itself that exhibits zero shear stress with high shear gradients in opposing directions and increasing stenosis severity as a result of flow separation. The ECs within the stenosis throat are shown to be exposed to very high WSS and a high shear gradient with direction reversal that varies dynamically as a function of the cardiac cycle.

MATERIALS AND METHODS

Stenosis Geometry and Computational Mesh Generation

Vessel model dimensions were based on a 4-mm luminal diameter, which is similar to that in humans within the proximal intracranial internal carotid artery and the proximal coronary artery. A straight tube was modeled using Autodesk 3DS Max software (Autodesk; San Rafael, CA) with an overall length of 120 mm. Axisymmetric stenoses of increasing severity were generated (*Fig. 1A*). The midpoint of the stenosis was kept 50 mm from the inflow to ensure sufficient length (10 diameters) for the full development of a Womersley profile, which describes the blunted profile of flow in blood vessels as a result of the pulsatile pressure that drives the flow (51). A smooth stenosis tapering over 1 cm was modeled with smooth sinusoidal inflow and outflow and varying degrees of severity, namely, 25, 50, and 75% reduction of diameter (in accordance with North American Symptomatic Carotid Endarterectomy Trial criteria [2]), which correspond to 44, 75, and 94% reductions in each cross-sectional area, respectively.

A hybrid, predominantly hexahedral, tetrahedral-hexahedral mesh was generated via a semiautomated process. A typical mesh (grid) contained 450,000 cells, and cell volume ranged from 0.0001 to 0.01 mm^3. Boundary-layer enrichment was used to increase the density of smaller-sized cells next to the wall to improve the computation accuracy of WSS and its gradient (refer to the *Appendix* for details).

Computational Fluid Dynamic Analysis

The computational analysis was carried out assuming a laminar flow model and using Fluent version 6.2.16 software (Fluent, Lebanon, NH) (18) on a cluster of parallel computers in the Windows environment (Windows versions XP64 and XP; Microsoft Corp., Redmond, WA).

Blood was modeled with a density of $\rho = 1.06$ g/mL as a non-Newtonian fluid to better simulate the known shear-rate dependence of its viscosity (11, 48, 49). In large blood vessels, the non-Newtonian properties of blood can be represented mainly by its shear-thinning properties (decreasing viscosity with increasing shear rate), and its viscoelastic properties may be ignored to simulate flow dynamics (25, 26). The shear-thinning properties of blood were captured using the Carreau-Yasuda model (6); its parameters were derived from a best fit to experimental data obtained on blood analog fluid (25, 26). *Figure 1B* shows the relationship between dynamic viscosity and shear rate. (Refer to the *Appendix* for a detailed description of the parameters of the Carreau-Yasuda model.) Steady-state simulations for the model validation assuming Newtonian behavior of blood were performed using a viscosity value of 3.6014 cP (1).

In the present, idealized model, the boundary conditions were chosen to provide physiologically relevant geometric dimensions and flow values. Time-varying pulsatile flow was obtained using a 100-step physiological flow profile that prescribed the inlet velocity, which allowed the development of a fully developed Womersley (51) velocity profile with Reynolds numbers (Re) of 140 at average velocity and 459 at peak systolic velocity in the prestenotic segment. We employed an inlet velocity temporal waveform that was averaged from normal human carotid waveforms (29) and scaled in such a way that the time-averaged velocity resulted in a mean WSS of 15 to 20 dyn/cm^2 in the prestenotic segment. The average inlet velocity was 0.22 m/s (*Fig. 1C*).

The vessel wall was assumed to be rigid, and velocity conditions obeyed nonslip and nonpenetration constraints at the wall. The computational approach was validated using experimental data that was previously reported by Ahmed and Giddens (1); the validation and comparison to those experimental data are shown in the *Appendix*. In addition, independence of the computed results from grid resolution, inlet flow conditions, and periodicity were similarly confirmed (see *Appendix*). Postprocessing was performed using Ensight software (version 8; Computational Engineering International, Apex, NC).

RESULTS

Flow Separation and Recirculation at Moderate Stenosis

(see videos at web site)

Streamline trajectories and instantaneous velocity vectors were used to illustrate the path of particles released from the inlet and allow a comprehensive illustration of the pattern of flow through the stenosis (*Fig. 2A*). During peak systole of the velocity profile (inlet flow rate of 7.6 mL/s) and at 25% stenosis (*Fig. 2A*) a small zone of recirculation was noted to form, but overall there was no significant variation from purely laminar flow. This zone is delineated proximally by the onset

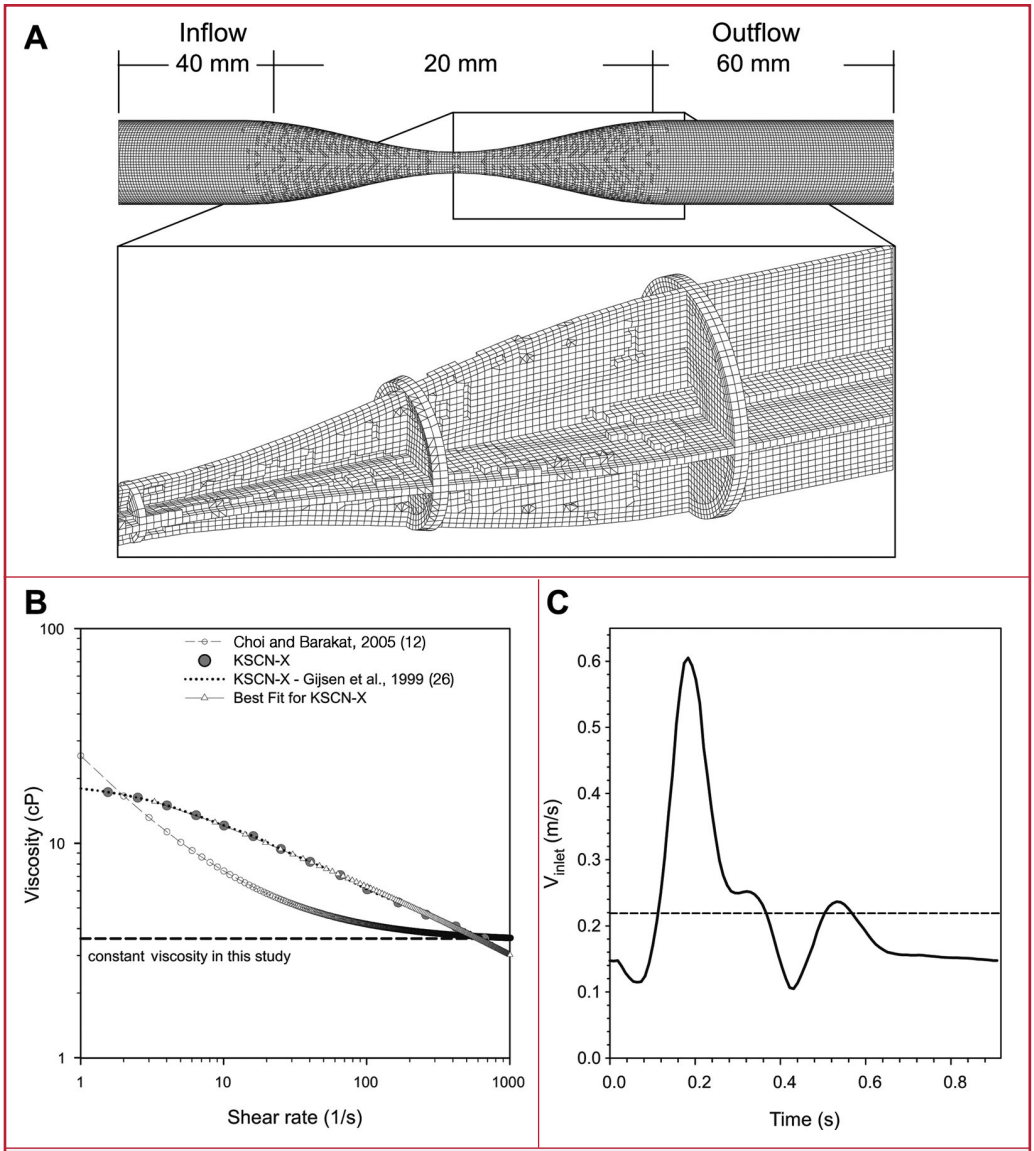


FIGURE 1. A, *schematic of the idealized stenosis model with external view of the computational mesh at 75% stenosis (inflow and outflow segments not to scale) and magnified triaxial cross-sectional view through the stenosis showing boundary-layer enrichment near the wall.* **B**, *dynamic viscosity as a function of shear rate for the Carreau-Yasuda model with different model parameters. Experimental data for xanthan gum mixed in potassium cyanate (KSCN-X) and its best fit as used in the present study are shown. Fits described by Gijsen et al. (26) and the Carreau model used by Choi and Barakat (12) are also indicated.* **C**, *inlet velocity (V) profile (*adapted from, *Holdsworth DW, Norley CJ, Frayne R, Steinman DA, Rutt BK: Characterization of common carotid artery blood-flow waveforms in normal human subjects.* ***Physiol Meas*** *20:219–240, 1999 [29]).*

of flow separation (as shown by the proximal arrowhead in *Fig. 2, A* and *B*), where the flow splits into antegrade central and retrograde peripheral components, and distally by the reattachment point (indicated by the distal arrowhead in *Fig. 2, A* and *B*), where the retrograde component disappears and the antegrade flow component again adheres to the wall. Increasing the degree of stenosis to 50 and 75% while keeping the flow rate constant (*Fig. 2A*) resulted in a larger recirculation zone that is illustrated by closed-path trajectories in the distal stenosis and poststenotic regions and a more distal reattachment point for 50 and 75% stenosis, as shown in *Figure 2B*.

Increasing stenosis led to increased flow velocity in a centripetal fashion, accentuating the normal velocity profile that is found in laminar flow. Axial cross-sectional velocity profiles (*Fig. 2B*) also demonstrate the simultaneous development of higher central peak velocity and greater retrograde flow velocity near the wall that occurred with increasing stenosis severity. The transition to recirculation in the poststenotic region was studied in greater detail by examining a longitudinal cross-section through the stenosis (*Fig. 2A*). For a 25% stenosis, the local flow vector smoothly follows the contour of the vessel, and a small zone of recirculation forms at the end of the stenosis (*Fig. 2A*). For a 50% stenosis, a transition to retrograde flow emerges that begins within the distal stenosis (as indicated by the arrowhead on *Fig. 2A*). For a 75% stenosis, the onset of the area of flow separation lies even more proximal and is located clearly within the stenosis rather than in the poststenotic region (shown by the arrowhead on *Fig. 2A*). The computed pressure decreases across the stenosis at peak systole were found to be 1.5, 5.9, and 93.5 mmHg at 25, 50, and 75% stenosis, respectively.

Use of boundary-layer enrichment allowed for consistent computation of the shear-stress vector at the wall (*Fig. 2C*). Approaching the throat of the stenosis from the inflow at 50% stenosis and peak systole, WSS increases dramatically in amplitude and exceeds 800 dyn/cm^2 in the center of the stenosis before it suddenly decreases to zero (*Fig. 2C*) approximately two-thirds of the way into the stenosis, and

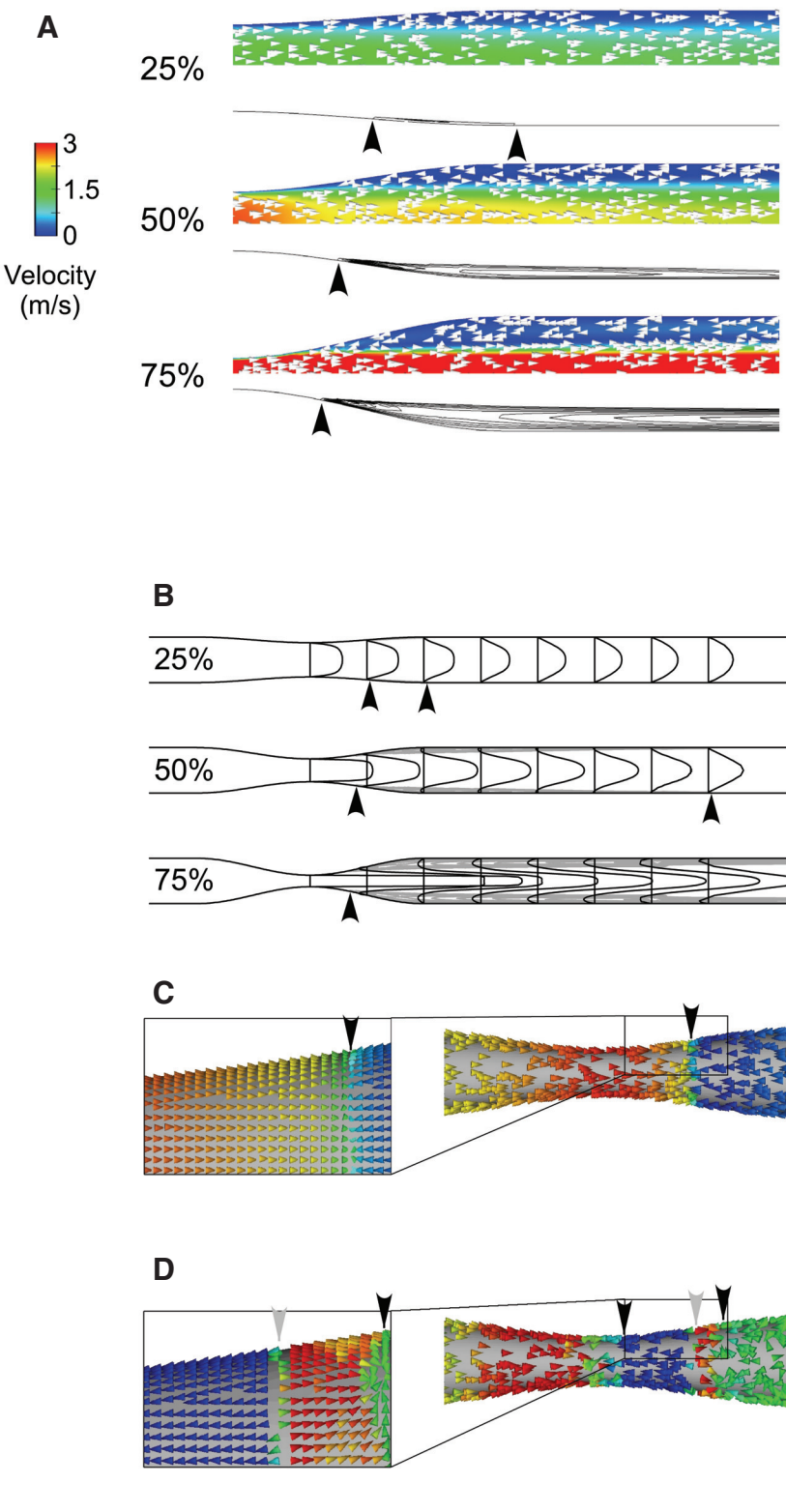


FIGURE 2. **A**, *color-coded longitudinal section showing the local flow velocity magnitude, and overlying arrows representing the local velocity vectors and path trajectories for the zone of retrograde flow for 25, 50, and 75% stenosis during peak systole.* Black arrowheads *denote the onset of flow separation with recirculation, and the reattachment point (shown for 25% stenosis only). See also Video 1 for velocity vector animation.* **B**, *cross-sectional view of the stenosis. Flow velocity contour occurs at different points from midstenosis onward with increasing stenosis severity, illustrating the development of retrograde flow in the recirculation zone (delineated by* arrowheads*).* **C**, *WSS vectorial representation on the inner luminal surface showing direction of the shear vector and color encoding to magnitudes at peak systole and 50% stenosis.* Arrowhead *indicates a transition point of zero shear within the distal stenosis.* **D**, *WSSG vectorial representation on the inner luminal surface at peak systole and 50% stenosis.* Arrows *represent WSSG vector direction and are color coded for magnitude.* Black arrowheads *indicate a point of convergent WSSG, and* the gray arrowhead *shows a point of divergent WSSG within the stenosis.*

then reverses direction from that point within the stenosis well into the poststenotic region. Analysis of the WSSG under the same conditions revealed several well-defined regions within the stenosis as one moves from the inflow through the stenosis; an initial antegrade WSSG in the direction of flow is followed by a retrograde WSSG that starts at the center of the stenosis, then another band of antegrade WSSG, and then a longer band of weaker retrograde WSSG at the end of the stenosis that decays into the poststenotic region (*Fig. 2D*). These four regions demarcate three important intervening bands of zero-valued WSSGs that are indicated by the arrowhead on *Figure 2D*; the first and last (*black arrowheads*) are characterized by convergent shear gradients, and the middle band (*gray arrowhead*) by a divergent shear gradient direction.

Effect of Stenosis Severity on Distribution of Wall Shear Stress and Its Gradient

The WSS pattern within the stenosis and the WSS magnitude were computed for varying degrees of stenosis at peak systole (*Fig. 3A*). At 25% stenosis, WSS is observed to increase within the stenosis before it returns to its baseline distally, and it remains purely antegrade in direction. At 50% stenosis a small segment near the exit of the stenosis exhibits negative WSS values, which correspond to retrograde WSS and recirculation. At 75% stenosis, a long segment is identified with negative WSS value that begins closer to the throat of the stenosis and extends for more than 20 mm. The peak antegrade WSS magnitude was measured at 364 dyn/cm^2 for 25% stenosis, 868 dyn/cm^2 for 50% stenosis, and 4243 dyn/cm^2 for 75% stenosis compared with 71 dyn/cm^2 in the healthy segment of the model (the time-averaged WSS in this segment over the cardiac cycle was 21 dyn/cm^2). Peak retrograde WSS values were measured as 92 dyn/cm^2 for 50% stenosis and 480 dyn/cm^2 for 75% stenosis.

The WSSG was computed and analyzed (*Fig. 3B*). An antegrade WSSG was observed immediately at the entrance of the stenosis as a result of flow acceleration and was followed by a peak proximal to the throat of the stenosis. At the throat, a reversal of WSSG direction occurred and was followed by a negative peak distal to the throat. The location of this peak was closer to the exit of the stenosis for lower degrees of stenosis. A second, smaller positive WSSG peak that was followed by a second negative peak could be identified for the 50% and 75% stenosis models. The peak WSSG was found to increase by more than one order of magnitude from 3.9×10^2 dyn/cm^3 for 25% stenosis to 8.8×10^3 dyn/cm^3 at 75% stenosis. The luminal surface corresponding to the endothelial lining within the stenosis model is therefore subjected to four distinct bands of opposing WSSG directions at high levels of stenosis. The junctions between these alternating WSSG bands denote a zone of convergent shear gradients at the throat of the stenosis that is followed by a point of divergent WSSGs; these junctions are located within the stenosis, and their location depends on the degree of stenosis (*Fig. 3B*).

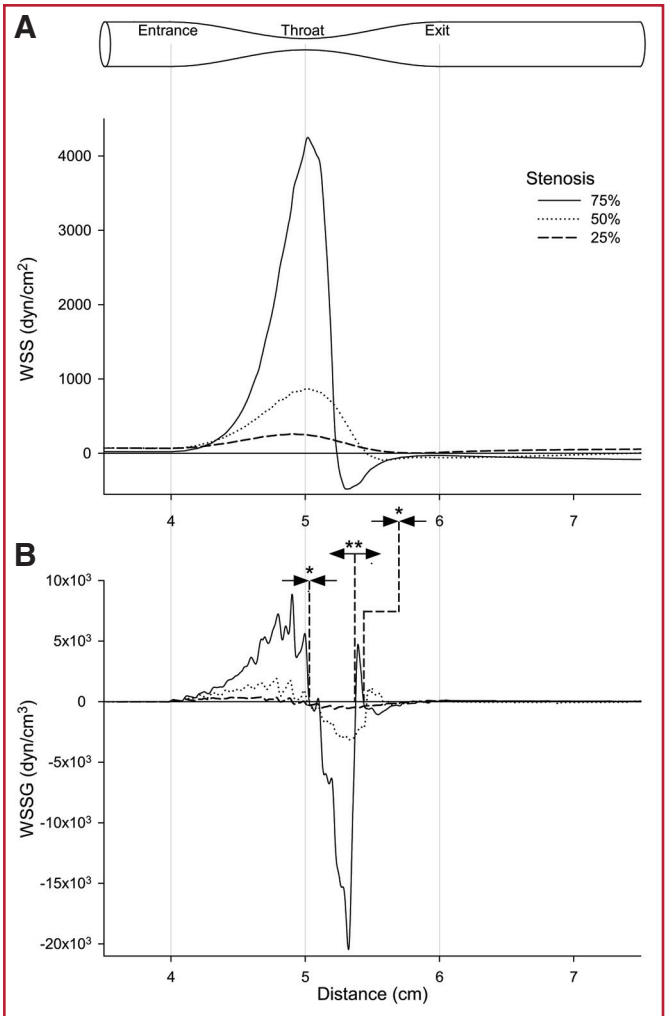


FIGURE 3. *Dependence of the peristenotic distribution of WSS (**A**) and WSSG (**B**) on increasing stenosis at a peak systolic flow rate, showing emergence of flow reversal and negative WSS within the distal stenosis even at moderate (50%) narrowing. Convergent (*) and divergent (**) shear gradients at the zero transition points are indicated.*

Time-dependent Migration of Shear-reversal Zone

(see videos at web site)

To better understand the time-dependent changes observed within a cardiac cycle, we examined the temporal changes of the profiles of WSS and WSSG under pulsatile flow through a 50% stenosis. At peak systole, the peak WSS was approximately five times greater than at diastole (868 dyn/cm^2 compared with 155 dyn/cm^2; see *Fig. 4*), with a steeper up-slope and a slightly more distal peak. The reversal to retrograde WSS occurred in the region between the throat and the exit of the stenosis. The location of shear reversal during peak systole was located halfway between the throat and the exit of the stenosis and moved approximately 4.4 mm closer to the throat during

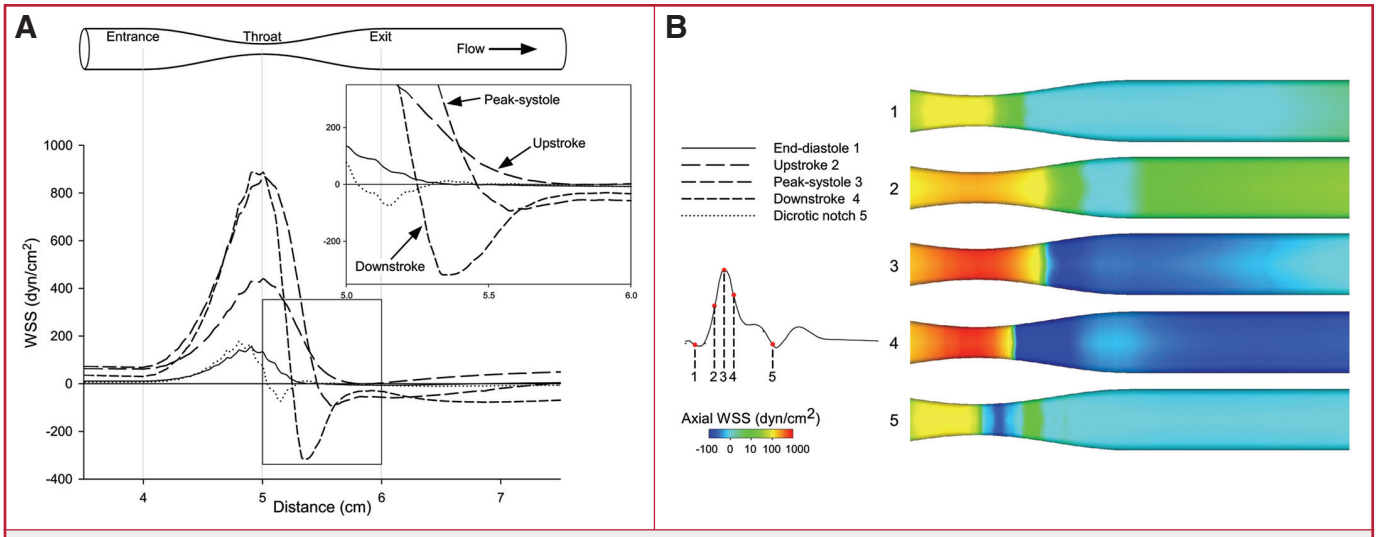


FIGURE 4. A, *temporal analysis of WSS changes for 50% stenosis during the five phases of the cardiac cycle; magnified* inset *shows detail of the dynamically varying shear reversal area within the distal stenosis.* **B**, *WSS spatial distribution is color coded for magnitude and direction during the five phases of pulsatile flow in a 50% stenosis. Also see Video 3 for animation of the WSS.*

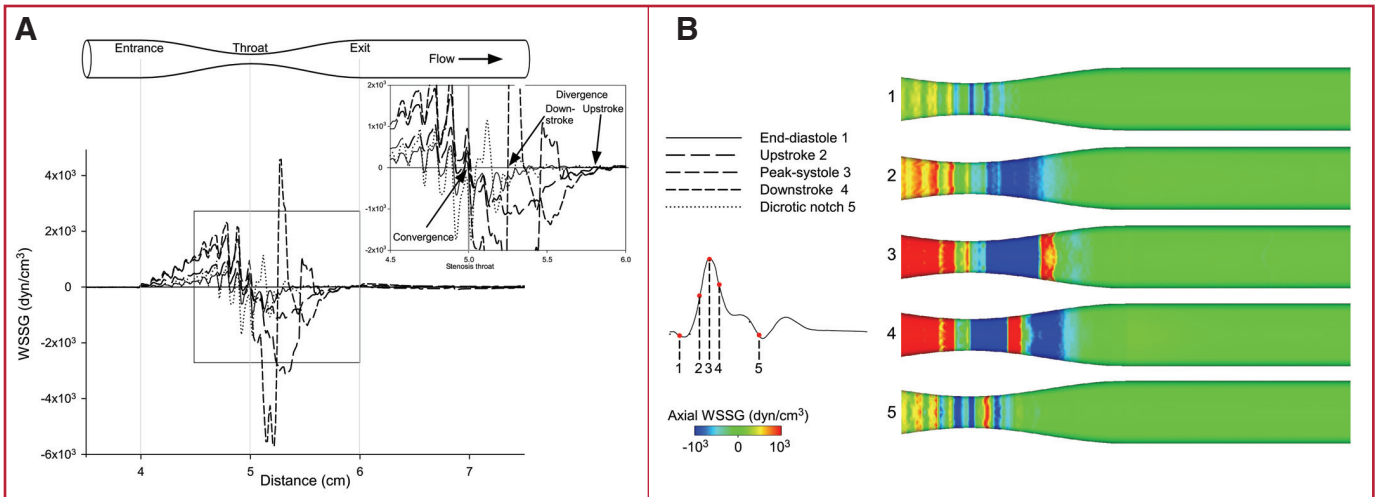


FIGURE 5. A, *temporal analysis of WSSG changes for a 50% stenosis during five phases of the cardiac cycle centered over the transition zones of WSSG within the distal stenosis.* **B**, *WSSG spatial distribution is color coded for magnitude and direction during the five phases of pulsatile flow in a 50% stenosis showing multiple regions of transition and banding. Also see Video 4 for animation of WSSG.*

downstroke and diastole. The location of shear reversal oscillated between these two extremes during the other phases of the pulsatile waveform (*Fig. 4*, *inset*); during end diastole and during the brief phase at the point of maximum acceleration, no retrograde WSS was observed. A second relative minimum and maximum of the retrograde WSS occurred more distally, thereby explaining the behavior of the WSSG (*Fig. 5*). A fourfold difference in the magnitude of WSSG arose between systole and diastole and exhibited the same bands of alternating positive and negative WSSG values, which correspond to antegrade and retrograde WSSG forces, respectively. The initial point of reversal of WSSG direction was convergent and shifted approximately 0.5 mm in the axial direction proximal to the throat of the stenosis (*Fig. 5*, *inset*). The subsequent downstream band of reversal from retrograde to antegrade WSSG oscillated over a 5.4-mm length between the extreme position closer to the throat during systole and a more distal position during diastole.

DISCUSSION

We used a model with shear-dependent thinning of viscosity to mimic the non-Newtonian properties of blood and capture the flow dynamics within a smooth stenosis of clinically mod-

erate severity. The findings reveal the onset of significant WSSGs in opposing directions within a stenosis as mild as 25%, and very high WSS in a 75% stenosis, which reached a value nearly three orders of magnitude higher than the baseline in the healthy prestenotic segment. In the clinical setting, the degree of stenosis is measured using North American Symptomatic Carotid Endarterectomy Trial criteria (2), whereas other workers in the field measure stenosis in terms of percent reduction in a cross-sectional area (1, 8, 10, 40, 50). To our knowledge, there are no data in the literature that examine a 75% North American Symptomatic Carotid Endarterectomy Trial stenosis (equivalent to 94% reduction in cross-sectional diameter) in detail under physiological flow conditions. Ahmed and Giddens (1) measured a 30-fold increase in WSS values to a maximum of 355 dyn/cm^2 for a 50% smooth axisymmetric stenosis. Buchanan et al. (8) did not report absolute values, but predicted a 13-fold increase in the peak WSS for a 50% stenosis, a finding that is comparable to our result of an approximately 12-fold increase from 74 to 867 dyn/cm^2 at peak systole.

The finding of a zero shear point within the stenosis proper with opposite shear vectors (*Fig. 2B, arrowhead*) is a key finding that differentiates the present analysis from previous sudden-expansion chamber models of stenosis. The appearance of sharply defined convergent and divergent WSSGs within the stenosis itself uncovers the potential for a hemodynamic microenvironment that can propagate a continued vicious cycle of EC mechanically induced dysfunction. Of equal importance is the finding that this region of zero shear migrates back and forth during the cardiac cycle, as does the region of associated gradient reversal, akin to a "scrubbing" motion. This effectively enlarges the region of the stenosis exposed to low WSS values with high spatial and temporal gradients; these features were previously shown to induce EC activation and an aggressive phenotype in vitro (21, 33, 43).

ECs have been shown to be functionally regulated by WSSGs in vitro (16), with up to a 25% rate of EC mitosis within the zone of reattachment associated with lower EC density in the region of disturbed flow. Tardy et al. (46) reported that a WSSG of 340 dyn/cm^3 led to high rates of proliferation within the area of high WSSGs, with EC migration and accumulation followed by EC detachment. The presence of a region within the stenosis itself that exhibits zero shear stress with convergent high WSSGs in opposing directions has significant implications on EC proliferation and turnover, and would imply the existence of an area of high EC density, whereas the downstream divergent area would yield an area of relatively low EC density and high turnover. There are few studies that highlight the effects of WSSG values greater than 10^2 dyn/cm^3 on EC function; the experimental in vitro setup of DePaola et al. (16) produced a peak WSSG estimated at only 600 dyn/cm^3. Such a WSSG, which is 15 times lower than that observed in the present study, led to significant EC functional modulation (16, 37, 46). This included increased nuclear localization of the transcription factors nuclear factor-κB, Egr-1, c-Jun, and c-Fos (37); increased mitosis; increased permeability (39); decreased EC-to-EC intercellular coupling; and persistent gap-junction disruption (15). WSSG values of 79 to 85 dyn/cm^3 were shown to decrease EC barrier function and increase transendothelial permeability to albumin by 5.5-fold as compared to a spatially uniform WSS (39). The migration and high turnover of ECs in the direction of the WSSG in vitro coupled with our findings suggest a migration and high turnover gradient for EC toward the center of the stenosis, with possible subsequent loss. Because EC activation has also been shown to increase with increasing WSSG (4), the results of the present study imply the presence of a microenvironment within even moderate stenoses that favors a cycle of EC migration and activation toward the center of the stenosis and may serve as a theoretical framework for continued progression of atherosclerosis in a positive-feedback model.

The transition point from laminar flow in a nonstenotic vessel or straight tube to more complicated flow dynamics including recirculation and turbulent features has been investigated in the past (10, 23). Most of these studies focused on the dynamics and behavior of the flow rather than the changes in wall shear forces or WSS magnitudes (1). The maximum velocity of 56 cm/s in the healthy segment of the vessel that was observed during peak systole in the present study is in concordance with values obtained from Doppler measurements of the intracranial internal carotid artery, a vessel that typically measures 4 mm in diameter (41). The baseline average WSS of 21 dyn/cm^2 upstream of the stenosis is also in good agreement with the expected range of WSS values in a normal artery. Compared with in vitro studies of ECs that have physiological WSS values in the 0–25 dyn/cm^2 range, few studies have described the effects of very high WSS (more than 100–200 dyn/cm^2); earlier studies by Fry (19) suggest that denudation of the canine aortic EC layer occurs with acute imposition of WSS greater than 379 dyn/cm^2. It is possible that a slower increase in WSS magnitude may help the ECs develop structural and functional adaptation to resist the high WSS observed in the 50% to 75% stenosis in our study. CFD techniques were recently studied (13) in healthy carotid bifurcation models using magnetic resonance angiography-mediated segmentation and modeling, and the in vivo regional variation in EC phenotype was confirmed. That study relied on CFD characterization of a disease-free carotid geometry (13). The much higher values of WSS and WSSG that are suggested by our study offer a starting point for the in vitro dissection of the EC response to pathological hemodynamics within clinically significant stenosis. The links between high WSSG and increased permeability (39) and high WSS values that are greater than the EC yield shear stress (19) may also indicate a relationship between stenosis and exposure of blood to the subendothelial thrombogenic extracellular matrix.

Non-Newtonian properties of blood were captured in our study with the Carreau-Yasuda model, using shear-thinning behavior as its dominant component and neglecting the viscoelastic properties (26). For the model of 25, 50, and 75% stenoses, the peak antegrade WSS values measured at peak systolic flow on the walls at the throats of the stenoses were

increased by 59, 5, and 6%, respectively, whereas no shifts in the location of the reversal points of WSS and WSSG were observed when the shear-thinning Carreau-Yasuda model was compared with a constant-viscosity model (data not shown). Our data suggest that assuming a Newtonian fluid (constant viscosity) results in underestimation of both WSS and its gradient (data not shown), which is consistent with previous studies that indicate non-Newtonian flows exhibit a more blunt velocity profile with higher resulting wall forces (8).

Although the axisymmetric smooth stenosis identified in this study is a simplification of the complex shapes observed in realistic vessel stenoses, it is similar to previous experimental models and thus allows for comparison with experimental data (1). The present model of an axisymmetric stenosis in a straight vessel is not suitable for modeling a carotid bifurcation; however, it is clinically applicable to smooth lesions of the cervical vertebral artery and the internal carotid artery beyond the carotid bifurcation, and to stenoses of straight segments of the intracranial vasculature. Other groups have used Reynolds-averaged techniques (such as the k-ε and k-ω models) (40, 50) that can model turbulence to study idealized axisymmetric stenoses, but these efforts have shown poor agreement with experimental results. More recently, direct numerical simulation has been used to achieve the same goal with better results (5). Our present computational approach can be applied to the study of irregular, patient-based, three-dimensional lesions, whose geometry can now be obtained using rotational angiography and multidetector computed tomographic angiography. Unlike the simple lesion in the present study, modeling of a realistic anatomy will result in complex tangential components of WSS and WSSG, and may result in high Re and turbulence for stenosis greater than 75%. Another limitation of the present analysis is its assumption of a rigid wall, whereas the vessel wall of a stenosis would be viscoelastic and would probably exhibit nonuniform spatial properties resulting from the complexity of plaque geometry and its heterogeneous material composition. Such an analysis would require the use of fluid-structure interaction techniques, whereby the computational mesh and its deformation by the prevailing pressure field is computed at each iteration and fed back to the CFD algorithm, resulting in a leap in computational requirement and complexity. Previous fluid-structure interaction analysis of a vessel stenosis (45) used a smaller grid size of 32,000 cells (compared with approximately 450,000 cells in our study), which would be insufficient to compute the spatiotemporal WSSG as presented in our study. Still, it is unclear whether the assumption of an elastic wall would fundamentally alter the basic premise of our findings. A recent study (31) comparing wall stress predictions in a model of an abdominal aortic aneurysm revealed only a 1% difference between the solid stress models and the elastic-wall (fluid-structure interaction) model.

In conclusion, the results of the present study suggest the presence of a microenvironment within moderate stenoses that favors continued EC activation and dysfunction not only within the poststenotic area, but also within the stenosis itself. This finding may serve as a framework for additional analysis of the functional response of ECs to the much higher levels of WSS and WSSG that appear to be prevalent in even moderate stenosis, and lead to improved understanding of the mechanism that leads to stenosis progression.

APPENDIX

Derivation of Carreau-Yasuda Model Parameters

Different rheological models have been used to simulate the non-Newtonian behavior of blood. The Carreau-Yasuda model has accurately described the properties of blood (26, 38, 42) and may be written as

$$\mu(\dot{\gamma}) = \mu_\infty + (\mu_0 + \mu_\infty)[1 + (\lambda\dot{\gamma})^2]^{(n-1)/2}$$

where μ_∞ and μ_0 designate the viscosity at infinite and zero shear rates, respectively, λ is the time constant of the shear-dependent viscosity changes, n is the index of the power law, and γ is the shear rate.

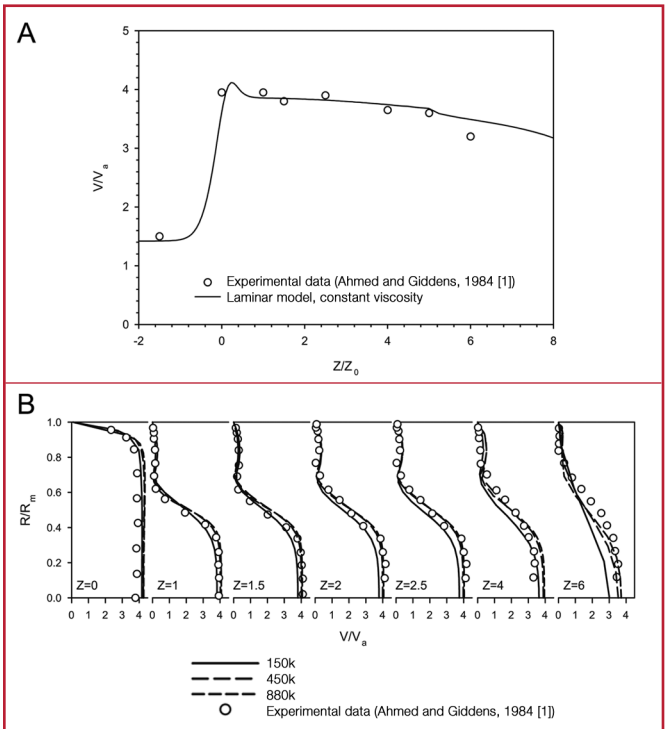


FIGURE 6. *Model validation.* **A**, *comparison of the computed centerline velocity in our model to experimental data previously reported by Ahmed and Giddens in 1984 (1).* **B**, *comparison of computed velocity profiles using our model with increasing grid density (results shown for 150,000, 450,000, and 880,000 cells) to previously reported experimental profiles at different axial locations downstream from the midpoint of the stenosis. V/V_a, ratio of the instantaneous centerline velocity (V) to the inlet centerline velocity (V_a); Z/Z_0, ratio of the axial distance from the midpoint of the stenosis (Z) over the baseline diameter of the vessel (Z_0) in its nonstenosed portion; R/R_m, relative distance from the centerline (ratio between the actual distance and the radius of the vessel at that point), accounting for the smaller radius of the vessel in the stenosis.*

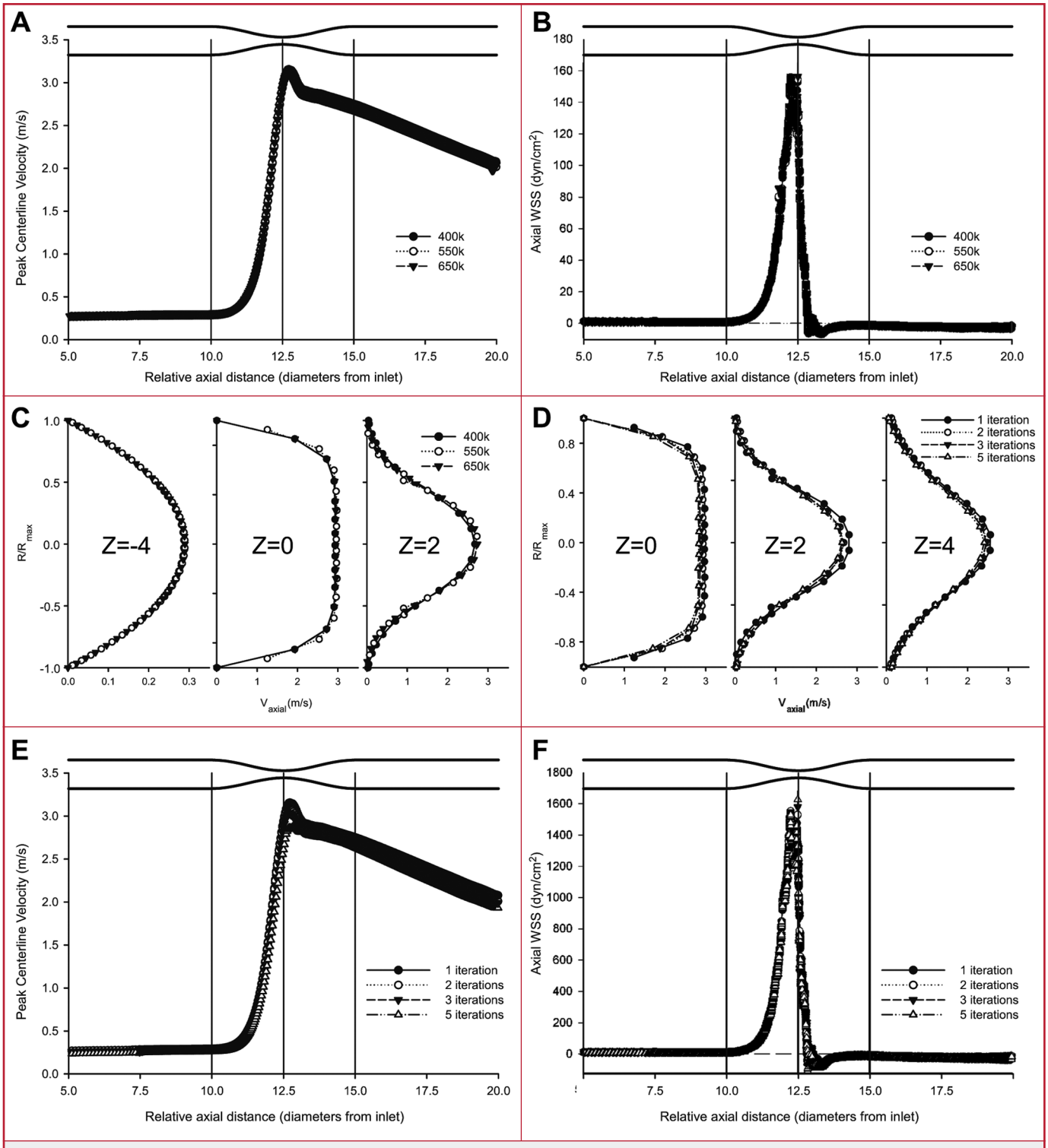


FIGURE 7. **A**, **B**, *and* **C**, *independence of flow velocity and WSS from grid density, showing results for 400,000, 550,000, and 650,000 cells.* **D**, **E**, *and* **F**, *independence from initial boundary conditions, illustrating results for one, two, three, and five iterations. Computed centerline velocity profile (***A*** and ***E***), estimated WSS profile (***B*** and ***F***), and axial velocity profiles (***C*** and ***D***) are shown. Axial velocity profiles were obtained at a distance of Z diameters relative to the throat of the stenosis (***C*** and ***D***).*

Experimental studies of the shear-thinning and viscoelastic properties of blood require a blood analog fluid that exhibits these non-Newtonian properties and additionally is transparent with a matched refractory index to allow for experimental analysis. Xanthan gum mixed in potassium cyanate has previously been shown to meet these requirements (26). Experimental data from Gijsen et al. (26) with the original fit (6) is shown in *Figure 1B* along with our best fit to their data, which closely mimics the dynamic viscosity of blood (26, 49). The best fit is achieved using the following model parameters: $\mu_\infty = 3.7$ cP (which corresponds closely to the viscosity value used for Newtonian simulations in this study, 3.6014 cP), $\mu_0 = 3.14$ cP, $\lambda = 2.517$ s, and $n = 0.5736$.

Our Carreau-Yasuda model compares closely to the fit of experimental data by Gijsen et al. (26) and deviates only for shear rates greater than 200/second (*Fig. 1B*). A model used by Choi and Barakat (12) that is known to intentionally underestimate the non-Newtonian properties of blood is shown for comparison.

Model Validation

We validated the results of our computational approach by comparing our results with the previously published experimental data of Ahmed and Giddens (1), who studied pulsatile flow through a tube with a diameter of 2 in and an axisymmetric smooth cosine-shaped stenosis with a 75% cross-sectional area reduction corresponding to a 50% reduction of the diameter (1). The inlet pulse is a sinusoidal pulse with a frequency of 0.005 Hz and a Re that varies between 200 and 1000 (mean Re, 600). The pulse was discretized into 80 time steps. In the original experimental setup, an entrance length of 96 diameters was used to ensure the development of the upstream flow. We reproduced the Ahmed and Giddens (1) geometry and boundary conditions using our computational model. In our validation model, however, we shortened the upstream length of the tube to 10 diameters, which still allowed for the generation of a fully developed velocity profile before the stenosis. The key flow parameters used to simulate the original experimental setup are mean velocity $U_0 = 0.04254$ m/s, amplitude of the sinusoidal velocity waveform $U_m = 0.02808$ m/s, $\omega = 0.314$ rad/s, diameter = 0.0508 m, density of the blood analogy fluid (ρ) = 1000 kg/m^3, and viscosity (μ) = 3.6014 cP.

Figure 6A compares the peak systolic centerline velocity measured in the experimental model by Ahmed and Giddens (1) to the results of a simulation in our computational model using laminar flow and a constant viscosity. We were able to obtain reasonable agreement with the experimental data for the shape of the cross-sectional velocity profiles downstream of the stenosis (*Fig. 6B*). In contrast with the difference in profile shape between the 150,000- and 450,000-cell meshes, no discernable difference was seen in the results from the 450,000- and 880,000-cell meshes.

In an attempt to model turbulence such as may occur during severe stenoses (greater than 75%) and/or at flow rates greater than those used in the present study, we used two computational models based on the Reynolds-averaged approach, k-ε and k-ω as implemented in Fluent. We found the results using both k-ε and k-ω to fit the experimental data of Ahmed and Giddens (1) poorly (data not shown), as previously reported (40, 50), and elected to limit our analysis to the nonturbulent regime.

Independence of Grid Parameters and Periodicity

We next evaluated the possibility of dependence of our computational approach on grid density, inlet boundary condition, and periodicity using the model of a 75% stenosis. Grids with 400,000 cells, 550,000 cells, and 650,000 cells were created, and the simulation was performed for three iterations of the cyclic inlet waveform. The centerline velocity magnitude, WSS, and axial velocity profiles at 4 diameters upstream, at the stenosis, and 2 diameters downstream were compared (see *Figure 7, A–C*). Little change was observed between the three grid densities (0.72% for centerline velocities, 1.7% for WSS, and 1.2% for axial velocity profiles), which suggests independence from grid density beyond a minimum number of 400,000 cells per grid. Three iterations of the cyclic inlet waveform (*Fig. 1C*) were sufficient to establish periodic independence of the initial flow boundary conditions. Small changes for the centerline velocity magnitude, WSS, and axial velocity profiles at the stenosis 2 and 4 diameters downstream were observed after two iterations compared to one iteration (see *Fig. 7, D–F*). Even smaller changes were observed when we compared two and three iterations (2.2% for centerline velocities, 2.4% for WSS, and 0.6% for axial velocity profiles), which justifies our choice to use three iterations in our computational analysis.

REFERENCES

1. Ahmed SA, Giddens DP: Pulsatile poststenotic flow studies with laser Doppler anemometry. **J Biomech** 17:695–705, 1984.
2. Anonymous: Beneficial effect of carotid endarterectomy in symptomatic patients with high-grade carotid stenosis. North American Symptomatic Carotid Endarterectomy Trial Collaborators. **N Engl J Med** 325:445–453, 1991.
3. Asakura T, Karino T: Flow patterns and spatial distribution of atherosclerotic lesions in human coronary arteries. **Circ Res** 66:1045–1066, 1990.
4. Bao X, Lu C, Frangos JA: Temporal gradient in shear but not steady shear stress induces PDGF-A and MCP-1 expression in endothelial cells: Role of NO, NF kappa B, and egr-1. **Arterioscler Thromb Vasc Biol** 19:996–1003, 1999.
5. Beratlis N, Balaras E, Parvinian B, Kiger K: A numerical and experimental investigation of transitional pulsatile flow in a stenosed channel. **J Biomech Eng** 127:1147–1157, 2005.
6. Bird RB, Armstrong RC, Hassager O: *Dynamics of Polymeric Liquids*. New York, Wiley, 1987.
7. Botnar R, Rappitsch G, Scheidegger MB, Liepsch D, Perktold K, Boesiger P: Hemodynamics in the carotid artery bifurcation: A comparison between numerical simulations and in vitro MRI measurements. **J Biomech** 33:137–144, 2000.
8. Buchanan JR, Kleinstreuer C, Comer JK: Rheological effects on pulsatile hemodynamics in a stenosed tube. **Comput Fluids** 29:695–724, 2000.
9. Calamante F, Yim PJ, Cebral JR: Estimation of bolus dispersion effects in perfusion MRI using image-based computational fluid dynamics. **Neuroimage** 19:341–353, 2003.
10. Cassanova RA, Giddens DP: Disorder distal to modeled stenoses in steady and pulsatile flow. **J Biomech** 11:441–453, 1978.
11. Chien S, Usami S, Dellenback RJ, Gregersen MI: Shear-dependent deformation of erythrocytes in rheology of human blood. **Am J Physiol** 219:136–142, 1970.
12. Choi HW, Barakat AI: Numerical study of the impact of non-Newtonian blood behavior on flow over a two-dimensional backward facing step. **Biorheology** 42:493–509, 2005.

13. Dai G, Kaazempur-Mofrad MR, Natarajan S, Zhang Y, Vaughn S, Blackman BR, Kamm RD, Garcia-Cardena G, Gimbrone MA Jr: Distinct endothelial phenotypes evoked by arterial waveforms derived from atherosclerosis-susceptible and -resistant regions of human vasculature. **Proc Natl Acad Sci USA** 101:14871–14876, 2004.
14. De Keulenaer GW, Chappell DC, Ishizaka N, Nerem RM, Alexander RW, Griendling KK: Oscillatory and steady laminar shear stress differentially affect human endothelial redox state: Role of a superoxide-producing NADH oxidase. **Circ Res** 82:1094–1101, 1998.
15. DePaola N, Davies PF, Pritchard WF Jr, Florez L, Harbeck N, Polacek DC: Spatial and temporal regulation of gap junction connexin43 in vascular endothelial cells exposed to controlled disturbed flows in vitro. **Proc Natl Acad Sci USA** 96:3154–3159, 1999.
16. DePaola N, Gimbrone MA Jr, Davies PF, Dewey CF Jr: Vascular endothelium responds to fluid shear stress gradients. **Arterioscler Thromb** 12:1254–1257, 1992.
17. Dimmeler S, Hermann C, Galle J, Zeiher AM: Upregulation of superoxide dismutase and nitric oxide synthase mediates the apoptosis-suppressive effects of shear stress on endothelial cells. **Arterioscler Thromb Vasc Biol** 19:656–664, 1999.
18. Fluent: *FLUENT 6.2 User's Guide.* Lebanon, Fluent, Inc., 2005.
19. Fry DL: Acute vascular endothelial changes associated with increased blood velocity gradients. **Circ Res** 22:165–197, 1968.
20. Fukushima T, Azuma T: The horseshoe vortex: A secondary flow generated in arteries with stenosis, bifurcation, and branchings. **Biorheology** 19:143–154, 1982.
21. Garcia-Cardena G, Comander J, Anderson KR, Blackman BR, Gimbrone MA Jr: Biomechanical activation of vascular endothelium as a determinant of its functional phenotype. **Proc Natl Acad Sci USA** 98:4478–4485, 2001.
22. Ghalichi F, Deng X, De Champlain A, Douville Y, King M, Guidoin R: Low Reynolds number turbulence modeling of blood flow in arterial stenoses. **Biorheology** 35:281–294, 1998.
23. Giddens DP, Mabon RF, Cassanova RA: Measurements of disordered flows distal to subtotal vascular stenoses in the thoracic aortas of dogs. **Circ Res** 39:112–119, 1976.
24. Giddens DP, Zarins CK, Glagov S: The role of fluid mechanics in the localization and detection of atherosclerosis. **J Biomech Eng** 115:588–594, 1993.
25. Gijsen FJ, Allanic E, van de Vosse FN, Janssen JD: The influence of the non-Newtonian properties of blood on the flow in large arteries: Unsteady flow in a 90 degrees curved tube. **J Biomech** 32:705–713, 1999.
26. Gijsen FJ, van de Vosse FN, Janssen JD: The influence of the non-Newtonian properties of blood on the flow in large arteries: Steady flow in a carotid bifurcation model. **J Biomech** 32:601–608, 1999.
27. Gimbrone MA Jr, Resnick N, Nagel T, Khachigian LM, Collins T, Topper JN: Hemodynamics, endothelial gene expression, and atherogenesis. **Ann N Y Acad Sci** 811:1–11, 1997.
28. Glor FP, Ariff B, Crowe LA, Hughes AD, Cheong PL, Thom SA, Verdonck PR, Firmin DN, Barratt DC, Xu XY: Carotid geometry reconstruction: A comparison between MRI and ultrasound. **Med Phys** 30:3251–3261, 2003.
29. Holdsworth DW, Norley CJ, Frayne R, Steinman DA, Rutt BK: Characterization of common carotid artery blood-flow waveforms in normal human subjects. **Physiol Meas** 20:219–240, 1999.
30. Kohler U, Marshall I, Robertson MB, Long Q, Xu XY, Hoskins PR: MRI measurement of wall shear stress vectors in bifurcation models and comparison with CFD predictions. **J Magn Reson Imaging** 14:563–573, 2001.
31. Leung JH, Wright AR, Cheshire N, Crane J, Thom SA, Hughes AD, Xu Y: Fluid structure interaction of patient specific abdominal aortic aneurysms: A comparison with solid stress models. **Biomed Eng Online** 5:33, 2006.
32. Long Q, Xu XY, Ariff B, Thom SA, Hughes AD, Stanton AV: Reconstruction of blood flow patterns in a human carotid bifurcation: A combined CFD and MRI study. **J Magn Reson Imaging** 11:299–311, 2000.
33. Malek AM, Alper SL, Izumo S: Hemodynamic shear stress and its role in atherosclerosis. **JAMA** 282:2035–2042, 1999.
34. Malek AM, Izumo S: Mechanism of endothelial cell shape change and cytoskeletal remodeling in response to fluid shear stress. **J Cell Sci** 109:713–726, 1996.
35. Mazzolai L, Silacci P, Bouzourene K, Daniel F, Brunner H, Hayoz D: Tissue factor activity is upregulated in human endothelial cells exposed to oscillatory shear stress. **Thromb Haemost** 87:1062–1068, 2002.
36. Moore JA, Steinman DA, Holdsworth DW, Ethier CR: Accuracy of computational hemodynamics in complex arterial geometries reconstructed from magnetic resonance imaging. **Ann Biomed Eng** 27:32–41, 1999.
37. Nagel T, Resnick N, Dewey CF Jr, Gimbrone MA Jr: Vascular endothelial cells respond to spatial gradients in fluid shear stress by enhanced activation of transcription factors. **Arterioscler Thromb Vasc Biol** 19:1825–1834, 1999.
38. Perktold K, Resch M, Florian H: Pulsatile non-Newtonian flow characteristics in a three-dimensional human carotid bifurcation model. **J Biomech Eng** 113:464–475, 1991.
39. Phelps JE, DePaola N: Spatial variations in endothelial barrier function in disturbed flows in vitro. **Am J Physiol Heart Circ Physiol** 278:H469–H476, 2000.
40. Ryval J, Straatman AG, Steinman DA: Two-equation turbulence modeling of pulsatile flow in a stenosed tube. **J Biomech Eng** 126:625–635, 2004.
41. Saqqur M, Demchuk AM, Hill MD, Dean N, Schebel M, Kennedy J, Barber PA, Shuaib A: Bedside emergency transcranial Doppler diagnosis of severe carotid disease using orbital window examination. **J Neuroimaging** 15:138–143, 2005.
42. Seo T, Schachter LG, Barakat AI: Computational study of fluid mechanical disturbance induced by endovascular stents. **Ann Biomed Eng** 33:444–456, 2005.
43. Stone PH, Coskun AU, Kinlay S, Clark ME, Sonka M, Wahle A, Ilegbusi OJ, Yeghiazarians Y, Popma JJ, Orav J, Kuntz RE, Feldman CL: Effect of endothelial shear stress on the progression of coronary artery disease, vascular remodeling, and in-stent restenosis in humans: In vivo 6-month follow-up study. **Circulation** 108:438–444, 2003.
44. Stroud JS, Berger SA, Saloner D: Numerical analysis of flow through a severely stenotic carotid artery bifurcation. **J Biomech Eng** 124:9–20, 2002.
45. Tang D, Yang C, Kobayashi S, Ku DN: Steady flow and wall compression in stenotic arteries: A three-dimensional thick-wall model with fluid-wall interactions. **J Biomech Eng** 123:548–557, 2001.
46. Tardy Y, Resnick N, Nagel T, Gimbrone MA Jr, Dewey CF Jr: Shear stress gradients remodel endothelial monolayers in vitro via a cell proliferation-migration-loss cycle. **Arterioscler Thromb Vasc Biol** 17:3102–3106, 1997.
47. Thomas JB, Milner JS, Rutt BK, Steinman DA: Reproducibility of image-based computational fluid dynamics models of the human carotid bifurcation. **Ann Biomed Eng** 31:132–141, 2003.
48. Thurston GB: Frequency and shear rate dependence of viscoelasticity of human blood. **Biorheology** 10:375–381, 1973.
49. Thurston GB: Rheological parameters for the viscosity viscoelasticity and thixotropy of blood. **Biorheology** 16:149–162, 1979.
50. Varghese SS, Frankel SH: Numerical modeling of pulsatile turbulent flow in stenotic vessels. **J Biomech Eng** 125:445–460, 2003.
51. Womersley JR: Method for the calculation of velocity, rate of flow and viscous drag in arteries when the pressure gradient is known. **J Physiol** 127:553–563, 1955.

COMMENTS

Schirmer and Malek elegantly model an idealized stenosis of a 4 mm vessel. At 50% or greater stenosis, they observed a zone of zero shear stress bounded by opposite vector regions of high shear stress. The authors propose that this may represent a region of significant endothelial cell migration and activation within the stenosis itself that may create a positive feedback loop for atherosclerosis progression. Future work may be extended to model the more complex stenotic relationships within typically observed non-idealized stenoses in patients. The work should lay the foundation for a better understanding of forces contributing to both stenosis and restenosis after treatment in the carotid vasculature.

Bob Carter
Boston, Massachusetts

In this article, the authors use a time-dependent computational fluid dynamic analysis in a non-Newtonian model of blood to look at shear-dependent viscosity for the purpose of obtaining a computa-

tional model of wall shear stress (WSS) in the area of the stenosis approximating that which might be seen in the internal carotid or some of the larger intracranial vessels with atherosclerotic or post-dissection stenosis. The authors use complex calculation models to look at stenosis rates of 25, 50, and 75% by North American Symptomatic Carotid Endarterectomy Trial criteria (up to 94% area of reduction) and look at WSS. WSS has been seen to be an important parameter in the proliferation, phenotypic change, and sloughing of endothelial cells in areas of stenosis. The authors' study suggests that the WSS is dramatically increased with increases in stenosis and the location of the WSS. This study has two interesting features. The area of greatest stress is outside of the stenosis at the lower degrees of stenosis. But, at the higher flow stenosis, the area of WSS tends to migrate within the stenosis itself, suggesting a process that could change endothelial cells and their attempts to endothelialize in the plaque area. Two further important findings are the reversal of WSS within the stenosis at the high degree of stenosis and the cyclical pulsatile pattern. First, the reversal of WSS suggests that a node exists within the high-grade stenosis, which is followed by an area of negative shear stress. The effects of high, none, and then negative shear stress would cause local areas of endothelial change and even bulging of endothelial cells within the most stenotic area, factors which may be important for both obstruction of flow and embolization. The authors consider this to be one of their most important findings. A second finding is that when modeled on pulsatile cyclical flow, as during a cardiac heartbeat, the node or area of switch from positive to negative, WSS will move up and down the stenosis. This creates a potential "scrubbing" action moving up and down the inner surfaces of the plaque, which may profoundly accelerate the processes of endothelial cell injury and morphological and phenotypic change.

This study is extremely complex and needs significant explanation for its target audience. The introduction covers what is known about the relationship of WSS to endothelial cell growth, change, and morphology. The importance of studying the WSS within atherosclerosis and stenosis is an increasing area of study.

Finally, in the discussion, the authors suggest that the presence of an area within the throat of this high-grade stenosis with a reversal of shear stress in an area of zero WSS would be an area of endothelial cell proliferation and turnover or high density of cells. This is an important part of their thesis. However, this does not take into account their second finding that the pulsatile nature of cardiac output results in migration of this area up and down the plaque. This is a scrubbing motion, which is very different than any current seen in the laminar flow of a constant fluid. Therefore, the location of this node of zero wall stress moving may provide an additional complexity to the theories of endothelial cell morphological change and may indeed accelerate the process. The authors should explain and expand upon these findings.

Robert J. Dempsey
Madison, Wisconsin

The authors, who are well versed in fluid dynamics, have evaluated the effects of WSS on mild to moderate stenosis. They use a complex computational fluid model to evaluate the effects of this stenosis. As the authors state, this is important work as WSS is known to be integrally involved in regulating endothelial function. In this study, the authors have clearly demonstrated that stenosis is a dynamic process and even in moderate stenosis WSS is altered both distal to the stenotic lesion and, most importantly, within the lesion. Their finding may postulate that once a stenosis starts, its progression may just be a self-fulfilling prophecy.

Gavin W. Britz
Seattle, Washington

Using computational fluid dynamics, the authors modeled a stenotic vessel and analyzed the WSS gradient near the stenosis. A simplified model of a vessel was used with the assumptions of the vessel as a container with rigid walls with a nonslip condition and blood as a shear-thinning fluid. They found that there is a zone of divergent WSS gradient in the stenotic region, which shifts in conjunction with the cardiac cycle. The authors conclude that the motion of the region of the zero-shear stress with the cardiac cycle results in a "scrubbing" motion, which may result in endothelial cell activation and dysfunction.

The current model made a number of simplifying assumptions, including that of a rigid non-bifurcating pipe and an idealized smooth stenosis, and is limited to the non-turbulent regime, thereby rendering it suitable only for idealized straight segments of the extra- and intracranial vasculature that are at most moderately stenotic. However, such reductionist quantitative models are important and necessary starting points for the understanding of complex biological systems. That the authors were able to find a physical mechanism for endothelial cell dysfunction despite the simplicity of the model is remarkable. Undoubtedly, the continuation of this and other similar work will be able to provide further insight into vascular pathology.

Rose Du
Robert M. Friedlander
Boston, Massachusetts

In this study, Schirmer and Malek have analyzed the spatiotemporal changes of WSS and its gradient at mild to moderate stenoses by time-dependent computational fluid dynamic analysis using a non-Newtonian Carreau-Yasuda model of blood viscosity. Although there are some limitations, including the neglect of viscoelastic properties of blood and the assumption that the vessel wall is rigid, the experimental model itself is well-designed. They found a zone of zero-WSS and divergent WSS gradient within the stenosis under 75% stenosis by North American Symptomatic Carotid Endarterectomy Trial criteria. The zone of divergent WSS gradient shifted over the cardiac cycle. These results will help us understand the flow environment around the vessel stenosis.

Flow dynamics in the cervical and intracranial vascular disease can be analyzed by the computational fluid dynamic technique. However, it is still under debate how the changes in flow dynamics have an influence on the lesion progression. The authors measured the peak antegrade WSS in 75% stenosis at 4243 dyn/cm^2. However, what happens to the endothelium under such a high WSS has not yet been determined. Although the authors assume high turnover and migration of endothelial cells toward the throat of the stenosis, this cannot be directly linked to the progression of atherosclerosis. The pathophysiology of atherosclerosis is associated with chronic inflammation. Endothelial cells play a crucial role in the initiation of atherosclerosis by transcriptionally inducing various proinflammatory genes. However, the contribution of luminal endothelial cells to the progression of atherosclerosis has not yet been clarified. Unfortunately, data on computational fluid dynamic analysis cannot be applied to the clinical setting at present. We also have the same problem in the computational fluid dynamic study of intracranial aneurysms. It remains to be elucidated whether the rupture-prone point is subjected to low or high WSS. We must integrate the data obtained from fluid dynamic studies and biological data in order to utilize these data for our clinical work.

Hiroharu Kataoka
Nobuo Hashimoto
Kyoto, Japan